INDERSCIENCE PUBLISHERS
Linking academia, business and industry through research

International Journal of Machining and Machinability of Materials

ISSN online: 1748-572X - ISSN print: 1748-5711
https://www.inderscience.com/ijmmm

Experimental investigations into surface crack density and micro hole dimensions during ultrashort pulse laser ablation

P. Deepu, T. Jagadesh

DOI: 10.1504/IJMMM.2024.10067462

Article History:

Received:	27 April 2024
Last revised:	03 June 2024
Accepted:	22 June 2024
Published online:	18 March 2025

Experimental investigations into surface crack density and micro hole dimensions during ultrashort pulse laser ablation

P. Deepu and T. Jagadesh*

Department of Production Engineering,
National Institute of Technology,
Tiruchirappalli, India
Email: deepu9961@gmail.com
Email: jagadesh@nitt.edu
*Corresponding author

Abstract: In this work, an attempt has been made to understand the nested concentric and Z-path laser scanning paths interaction with thermal barrier coating (TBC) titanium alloy using ultrashort pulse laser. Ablation threshold is evaluated at various repetition rates (RR) and laser fluence for nested concentric and Z-path movement. Detailed investigations have been conducted to study the influence of RR, pulse overlap (PO), laser fluence, and the number of laser scans on surface crack density (SCD), hole diameter and depth. It is inferred that ablation threshold saturation is obtained after a critical RR of 20 kHz and 10 kHz for nested concentric and Z-path, respectively. Micro hole diameter and depth are highest at critical RR. Nested concentric scanning path movement provides better hole morphology than Z-path movement at 2.29 J/cm^2, however, the Z-path increased the hole depth by 25 µm at 1.78 J/cm^2.

Keywords: ultrashort pulse laser; surface crack density; SCD; laser ablation; hole diameter; hole depth; ablation threshold; thermal barrier coating; TBC.

Reference to this paper should be made as follows: Deepu, P. and Jagadesh, T. (2025) 'Experimental investigations into surface crack density and micro hole dimensions during ultrashort pulse laser ablation', *Int. J. Machining and Machinability of Materials*, Vol. 27, No. 1, pp.40–69.

Biographical notes: P. Deepu received his MTech in Production and Industrial Engineering from the Mahatma Gandhi University, India. He is currently perusing his PhD from National Institute of Technology, Tiruchirappalli, India. His research interest is laser micro-machining.

T. Jagadesh received his PhD and Post Doctoral Fellowship from the Indian Institute of Technology Madras, India. He is presently working as an Assistant Professor in National Institute of Technology Tiruchirappalli, India. His research interests are laser micromachining, mechanical micromachining, and composite 3D printing.

1 Introduction

In recent years, aircraft engine manufacturers have intended to improve the fuel efficiency and performance of the gas turbine by increasing the working temperature inside the engine (Niu et al., 2024; Clarke and Phillpot, 2005). Aero-engine components such as nozzle guide vanes, compressor blades, and turbine blades made of titanium alloy are widely used due to their superior performance at high temperatures, excellent corrosion resistance, and low density (Pawar et al., 2024; Perveen et al., 2020). These components operate at high temperatures near the melting temperature of the material to achieve high fuel efficiency (DeMasi-Marcin and Gupta, 1994). To withstand extreme temperatures and prevent the underlying material from reaching high temperature, the aero-engine parts are coated with thermal barrier coating (TBC) (Khadtare et al., 2020; Voisey and Clyne, 2004). Moreover, TBC is applied on the base material as a protective coating to protect the engine component from a corrosive and erosive environment, thereby improving the engine performance and service life of the components (DeMasi-Marcin and Gupta, 1994; Voisey and Clyne, 2004; Sun et al., 2019). The TBC consists of a thermally insulated ceramic layer of YSZ (yttria-stabilised zirconia) as a top coat and an underlying metallic oxidation-resistant bond coat, which is applied to the metallic substrate (Voisey and Clyne, 2004; Das et al., 2008; Bathe and Padmanabham, 2014).

Further enhancement in the engine performance and protect the engine components from high temperatures, surface cooling of TBC components is provided by drilling thousands of cooling micro holes extending from the top coat to the inner surface of the hollow component (Yeo et al., 1994; Meier and Gupta, 1992; McNally et al., 2004). These micro holes allow cool air to pass through and flow over the blade surface from the internal cooling channel, creating a protective cooling film layer, thereby enhancing the component service life. Drilling micro holes in TBC titanium alloy by mechanical micro-drilling leads to tool wear because of the differences in mechanical, chemical, and physical properties associated with multiple layers (Khadtare et al., 2020). Because of the electrically non-conducting characteristics of the TBC, non-traditional machining processes like electrochemical discharge machining and electrical discharge machining are not suitable for generating cooling holes (Li et al., 2015).

To overcome this limitation, an aircraft engine component manufacturer uses a non-contact laser micro-machining technique to drill thousands of cooling holes in the TBC components. A high-power laser beam removes the material through melt ejection or via vaporisation (Li et al., 2015). The practice of drilling micro-cooling holes in TBC components using long pulse length lasers, including millisecond and nanosecond, has recently been adopted by the aerospace sector. However, due to longer pulse duration associated with millisecond and nanosecond lasers, surface defects are seen around the machined area, including spatter, formation of recast layer, delamination along the interface of TBCs, heat affected zones (HAZ) and microcracks (Niu et al., 2024). These defects are not eliminated due to long pulse duration and will significantly affect the performance and life of aero-engine components (Bandyopadhyay et al., 2002; Biffi and Previtali, 2013; Feng et al., 2006).

During the past decade, the usage of ultrashort pulse laser (USP) became prevalent and commercialised due to shorter pulse duration and higher laser pulse energy. Due to the lesser time in laser-material interaction, heat dissipation to the surrounding material is

less, and direct solid-to-vapour transition occurs during the material ablation. As a result, collateral damage associated with USP laser is minimal (Das et al., 2008; Yu et al., 2019). Thus, the USP laser method can be exploited to generate high-quality holes in TBC engine components. Feng et al. (2006) investigated the micro-machining of nickel alloy coated with TBC utilising ultrashort laser. The hole taper formed at higher laser fluence, and thermal damages like micro-cracks, recast layer and HAZ, and obtained are less compared to conventional long pulsed laser (Feng et al., 2006). Das et al. investigated the geometrical characteristics of microholes drilled on TB-coated nickel based super alloy using an ultrafast laser. The results show that the obtained entrance hole diameter is 1.3 times more than the required diameter, having a maximum taper angle of 6º. Also, material damages like the recast layer and micro-cracks were observed on the YSZ coating (Das and Pollock, 2009). Lu et al. investigated the effect of laser power and laser focusing position to drill microholes on TBC nickel superalloy using a femtosecond laser. It was observed that higher laser power leads to poor hole roundness and causes it to deteriorate the microhole side wall (Lu et al., 2020).

The geometry and surface quality of microholes have a major impact on the performance of turbine blades (Zhang et al., 2020). The previous literature review indicates that, a less attempt has been made to investigate the effect of different ultrashort laser process parameters [in femtosecond regime (fs)] on the ablated hole morphology and geometry of TBC titanium alloy. Additionally, there is a substantial knowledge gap exists to understand the impact of different scanning modes on the diameter of the hole, depth, and density of micro-cracks after fs laser ablation. Hence, a systematic examination is required to understand the influence of fs laser process parameters in such as repetition rate (RR), pulse overlap (PO), laser fluence, and the number of repeat laser scans on the hole diameter, depth, surface crack density (SCD), and spatter deposition. The work aims to evaluate the ablation threshold fluence of TBC for nested concentric and Z-path scanning paths. Then, the influence of pulse overlap, repetition rate, laser fluence, and number of repeated laser scans on SCD and microhole dimensions for the ablated holes are investigated systematically for both the scanning path.

2 Experiment methods

In this experiment, Ti-6Al-4V having 0.5 mm thickness is taken as substrate material. Then the substrate sample is plasma spayed with NiCoCrAlY as a bond coat (Make: Sulzer Metco) and further with YSZ as a top layer. The top and bond layer have a thickness of 125 µm and 60 µm (Das and Pollock, 2009). The coating morphology and energy-dispersive spectroscopy (EDS) analysis of the thermal barrier coated Ti-6Al-4V are represented in Figure 1.

An ultrashort pulse laser operating in the femtosecond regime ablates microholes on TBC-coated titanium alloy. The closer view of experimental set-up of the femtosecond laser drilling center (Model – Femto IR 50-40, Make: Huaray) is demonstrated in Figure 2. The femtosecond laser utilised in this experiment has a pulse width, wavelength, and spot size of 350 fs, 1,035 nm, and 40 µm, respectively. A Z-path and nested concentric path is adopted to remove the material in the layer-wise method. In a nested concentric scanning path, the laser beam is initially concentrated at the centre of the pre-set hole. Later, the laser beam moves from the hole centre towards the hole circumference in a nested concentric way. While for the Z-path, the beam is focused

initially on the edge of the hole, moves in a linear path, followed by the Z movement, until it scans the complete geometry of the hole. Process parameters, such as RR, laser fluence, PO, and the number of repeated laser scans, are varied for nested concentric and Z-path to comprehend the fs laser interaction on TBC, as given in Table 1. The total of 60 experiments is performed by varying one process parameter at a time.

Figure 1 Coating morphology and EDS analysis of TBC layers, (a) and (b) represents a cross-section view of coating at 100 x and 500 x magnification, (c) EDS of top coat at area 1, (d) EDS of bond coat at area 2, (e) EDS of a substrate at area 3 (see online version for colours)

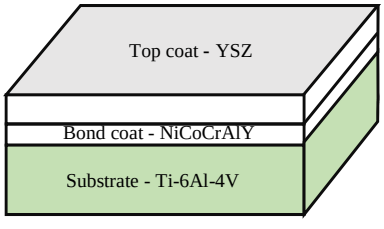

(a)

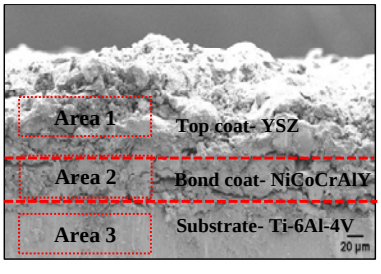

(b)

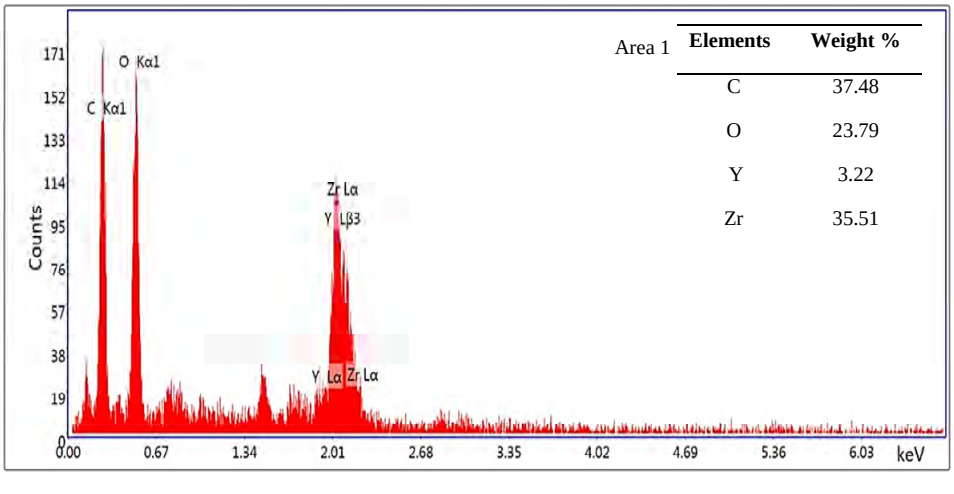

Area 1

Elements	Weight %
C	37.48
O	23.79
Y	3.22
Zr	35.51

(c)

Figure 1 Coating morphology and EDS analysis of TBC layers, (a) and (b) represents a cross-section view of coating at 100 x and 500 x magnification, (c) EDS of top coat at area 1, (d) EDS of bond coat at area 2, (e) EDS of a substrate at area 3 (continued) (see online version for colours)

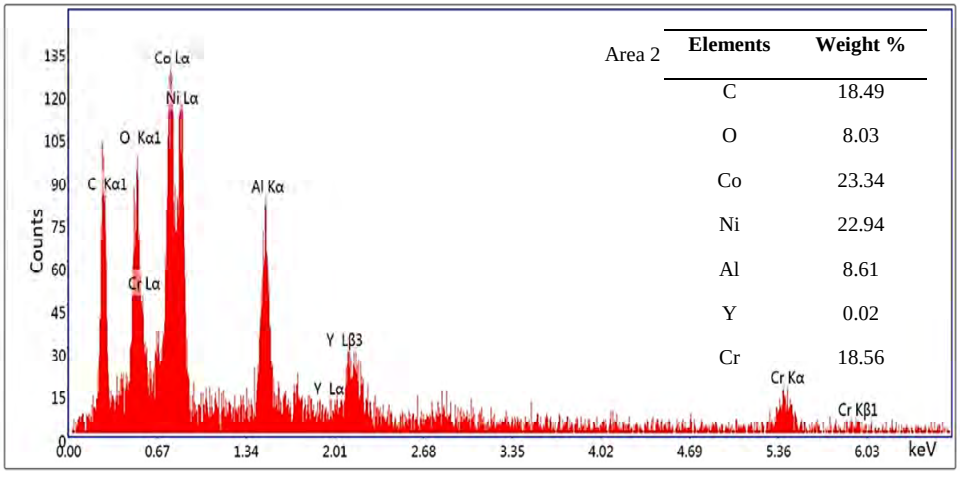

(d)

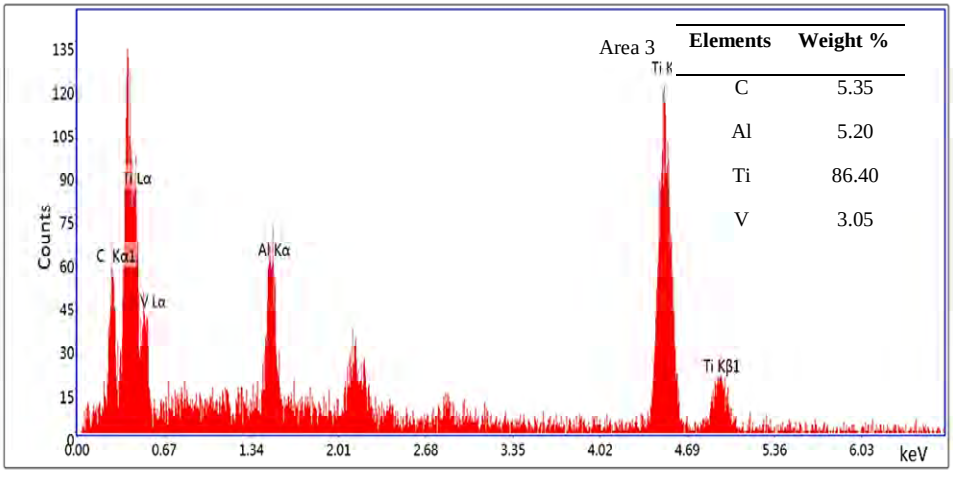

(e)

After drilling, the samples are ultrasonically cleaned with deionised water. The ablated diameter and depth were measured using an optical profiler. The diameter of the hole is measured by taking an average diameter measured along the periphery of the ablated hole at 45o intervals. For measuring the SCD, hole morphology is captured using scanning electron microscopy. The crack length is measured by analysing the SEM image using ImageJ software (open source). The SCD is evaluated by dividing the average length of the crack by the micrograph area (Parthiban et al., 2018; Bhattacharyya et al., 2007). The PO is evaluated for both the scanning modes using equation (1) (Liu et al., 2018).

$$\text{Pulse overlap(PO)} = \left(1 - \frac{v}{2f\omega}\right) \times 100\% \tag{1}$$

where ω is the spot diameter, v is the scanning speed, and f is the RR.

Figure 2 Closer view of experimental setup (see online version for colours)

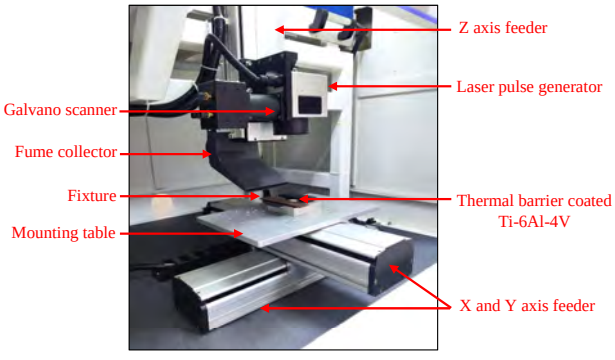

Table 1 Factors and levels for femtosecond laser ablation

Factors	*Levels for nested concentric and Z-path*
Laser fluence (J/cm^2)	1.78, 2.04, 2.29, 2.54
Repetition rate (kHz)	1, 5, 10, 20, 50, 75
Pulse overlap (%)	With overlap (75, 50, 25) and without overlap (0)
Number of repeated laser scans	1, 50, 100, 150, 200

3 Result and discussion

3.1 Determination of ablation threshold

The laser ablation of Ti-6Al-4V coated with TBC depends on laser control parameters, chemical and physical properties of different layers of TBC (Sun et al., 2019; Feng et al., 2006). The minimum fluence required to remove the material from the target surface is known as the ablation threshold. When the applied fluence exceeds the material ablation threshold, effective ablation occurs (Zhao et al., 2015). Therefore, determining the threshold of TBC is necessary for proper ablation. The ablation threshold fluence is evaluated using an empirical model developed by Liu for a laser beam with a Gaussian energy distribution profile (Liu, 1982). This model determines the ablation threshold by measuring the ablated diameter (Di Niso et al., 2014). The correlation between laser fluence and ablated diameter given in equation (2) is used to determine the ablation threshold of TBC (Zhai et al., 2017).

$$D^2 = 2\omega_0 \ln\left[\frac{\varphi_0}{\varphi_{th}}\right] \tag{2}$$

Here, D represents the average hole diameter, E_p is the laser pulse energy represented in equation (3), φ_{th} represents the laser ablation threshold and ω_0 is the laser spot size.

$$E_p = \frac{p}{f} \tag{3}$$

where P is the avg. laser power.

Peak laser fluence (φ_0) is evaluated using equation (4).

$$\varphi_0 = \frac{2E_p}{\pi\omega_0^2} \tag{4}$$

Figure 3 Ablation threshold vs. RR at various fluence for nested concentric and Z-path, (a) nested concentric path, (b) Z-path (see online version for colours)

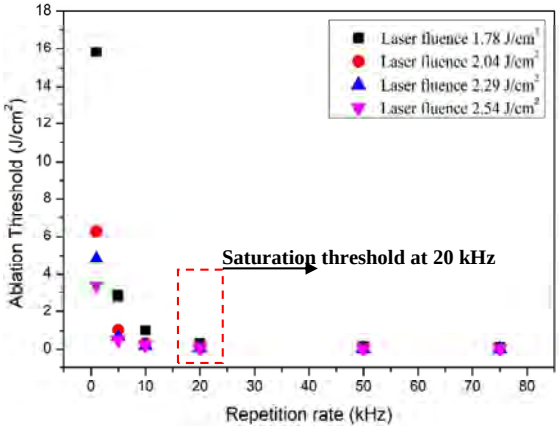

(a)

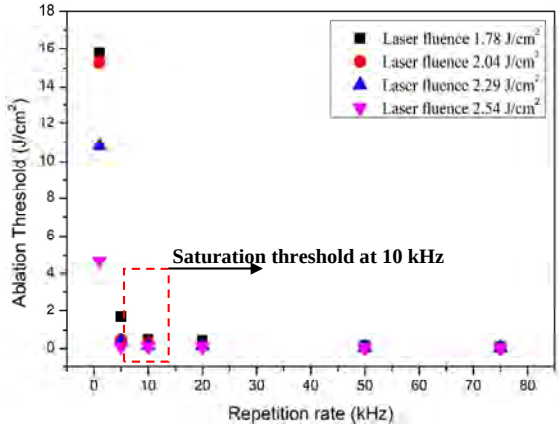

(b)

Table 2 Estimation of TBC ablation threshold path

S. no.	*Repetition rate (kHz)*	*Fluence – 1.78 J/cm²*		*Fluence – 2.04 J/cm²*		*Fluence – 2.29 J/cm²*		*Fluence – 2.54 J/cm²*	
		Ablation threshold fluence (J/cm²)							
		Nested concentric	*Z-path*	*Nested concentric*	*Z-path*	*Nested concentric*	*Z-path*	*Nested concentric*	*Z-path*
1	1	15.82	15.82	6.27	15.29	4.82	10.82	3.37	4.70
2	5	2.83	1.68	1.04	0.47	0.65	0.37	0.47	0.09
3	10	1.00	0.48	0.30	0.31	0.19	0.15	0.21	0.08
4	20	0.35	0.42	0.14	0.14	0.05	0.14	0.04	0.07
5	50	0.12	0.15	0.05	0.04	0.02	0.07	0.013	0.02
6	75	0.06	0.08	0.03	0.02	0.008	0.04	0.007	0.01

Table 2 represents the effect of RR on the ablation threshold of TBC for nested concentric and Z-path for different laser fluence. It is observed that the ablation threshold decreases abruptly till a critical repetition rate (CRR) of 20 kHz and 10 kHz is reached for nested concentric and Z-path. The decreasing trend in ablation threshold decelerates after CRR for both scanning paths.

Figure 3 shows a correlation between the ablation threshold and repetition rate for nested concentric and Z-path at various fluence. The threshold value of TBC decreases with an increase in RR from 1 kHz to 20 kHz for nested concentric path and from 1 kHz to 10 kHz for Z-path at various fluence, as illustrated in Figures 3(a) and 3(b), respectively. A significant decrease in threshold fluence is observed from 1.78 J/cm^2 for the nested concentric path, while for the Z-path, this decrease is noted from fluence levels of 1.78 and 2.04 J/cm^2, respectively. The surface condition at particular locations alters with increased RR, which leads to increased laser absorptivity, thereby decreasing the threshold fluence (Das et al., 2008). A similar trend is observed from 1 kHz to CRR, (i.e., 20 kHz for nested concentric and 10 kHz for Z-path) at 2.04, 2.29, and 2.54 J/cm^2 for nested concentric path and at 2.29 and 2.54 J/cm^2 for Z-path. After CRR, saturation in threshold value is observed for all the laser fluence with an increase in RR for both the scanning paths without any significant change in ablated diameter. This trend is comparable with the ultrashort laser hole drilling on TBC-coated nickel alloy (Liu et al., 2020).

Table 3 Variation of microhole dimensions and SCD with different laser fluence

S. no.	*Laser fluence (J/cm^2)*	*Scanning mode*	*Micro hole dimensions*		*Surface crack density (μm/μm^2)*
			Hole diameter (μm)	*Hole depth (μm)*	
1	1.78	Nested concentric	152	221	0.0034
		Z-path	154	246	0.00595
2	2.04	Nested concentric	169	238	0.0043
		Z-path	163	249	0.00987
3	2.29	Nested concentric	185	247	0.0066
		Z-path	179	257	0.0117
4	2.54	Nested concentric	189	248	0.0079
		Z-path	180	258	0.0119

3.2 Effect of laser fluence on SCD, morphology, and hole dimension

To study the influence of fluence on the hole diameter, depth, and SCD, the laser fluence is varied from 1.78 to 2.54 J/cm^2 for nested concentric and Z-path, as shown in Table 3. It is observed that an increase in fluence from 1.78 to 2.54 J/cm^2 and an increase in the diameter from 152 μm to 189 μm is obtained for nested concentric, whereas from 150 μm to 180 μm for Z-path, respectively. At 1.78 J/cm^2, as the laser pulse impinges on the surface of TBC, the top coat of TBC is slightly ablated due to the less laser energy being deposited on the material surface, leading to mild ablation, resulting in the vaporisation of material to form a smaller diameter hole without any melting for both the scanning path as depicted in Figures 4(a) and 4(b) (Li et al., 2022; Zhang et al., 2015).

Figure 4 Dependency of fluence on SCD and microhole dimension for various paths, (a) nested concentric path, (b) Z-path (see online version for colours)

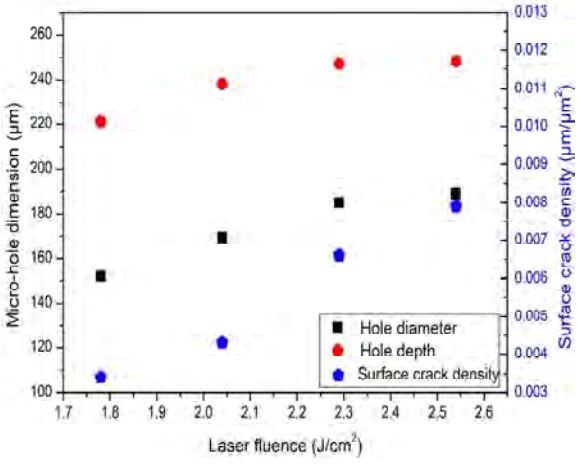

(a)

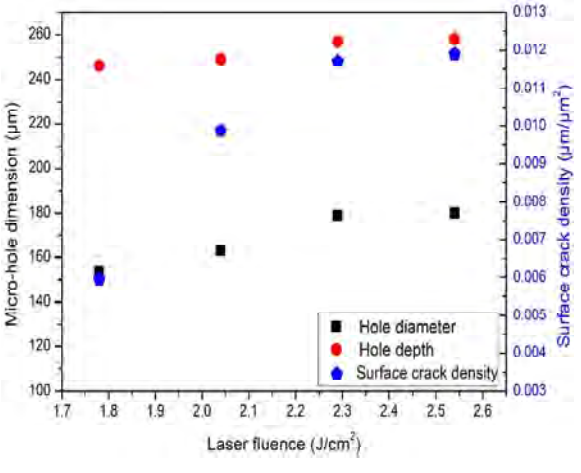

(b)

Furthermore, the diameter of nested concentric and Z-path paths increases with fluence from 2.04 to 2.29 J/cm^2, as more laser energy is imparted onto the workpiece, resulting in sudden rise of temperature due to strong ablation mechanism, characterised by mixing of vapour and liquid melt droplets under high pressure (Zhao et al., 2015). The rapid expansion of this high-pressure mixture prompts a sudden phase transition, facilitating substantial material removal from the TBC surface, thereby increasing the hole diameter (Kelly and Miotello, 1996). In addition, a linear relationship is noticed between the laser fluence and hole diameter from 1.78 to 2.29 J/cm^2 for Z-path and nested concentric paths, as shown in Figures 4(a) and 4(b), respectively. After 2.29 J/cm^2, an increasing trend in the hole diameter decelerates for both the scanning path due to the re-deposition of melted material on the hole periphery. A similar phenomenon is noticed during the laser

ablation of a blind hole in titanium carbide ceramic using an fs-pulsed laser (Zhang et al., 2015).

As shown in Figure 4, the micro hole depth increases with laser fluence. An increase in fluence from 1.78 to 2.54 J/cm^2 increased the hole depth from 221 µm to 248 µm for nested concentric and from 246 µm to 258 µm for Z-path, respectively. It could be seen that the hole depth increased significantly as fluence increased from 1.78 to 2.29 J/cm^2 for both scanning paths. Because electrons transfer energy to the bounded lattice electrons to form a high-temperature plasma plume over the material surface. Due to recoil pressure exerted by the plasma, the ablated material is ejected out completely to generate a deeper hole (Yu et al., 2019). In the Z-path, the hole depth obtained is higher than the nested concentric path by 25 µm at 1.78 J/cm^2 due to extra path movement, which leads to more material removal.

Figure 5 Surface topography of microhole, (a) at 2.54 J/cm^2, 50 kHz for nested concentric path (b) at 2.54 J/cm^2, 50 kHz for Z-path, (c) cross-section of the hole at 2.54 J/cm^2, 50 kHz for nested concentric path, (d) cross-section of the hole at 2.54 J/cm^2, 50 kHz for Z-path (see online version for colours)

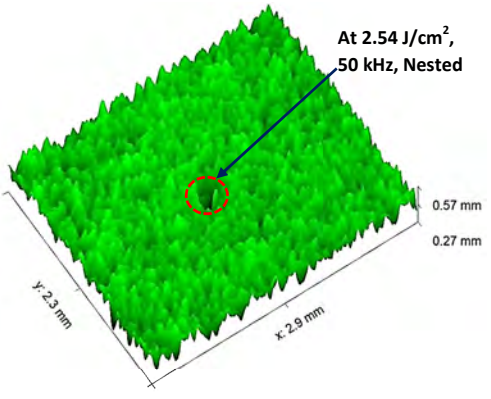

(a)

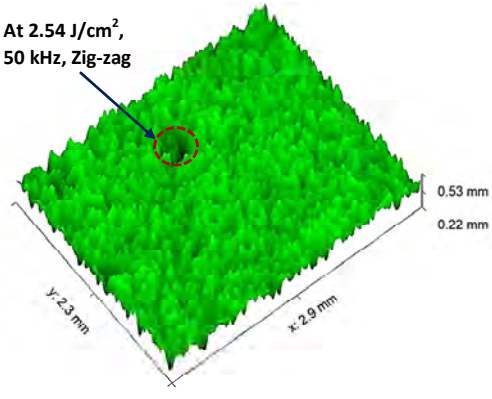

(b)

Figure 5 Surface topography of microhole, (a) at 2.54 J/cm^2, 50 kHz for nested concentric path (b) at 2.54 J/cm^2, 50 kHz for Z-path, (c) cross-section of the hole at 2.54 J/cm^2, 50 kHz for nested concentric path, (d) cross-section of the hole at 2.54 J/cm^2, 50 kHz for Z-path (continued) (see online version for colours)

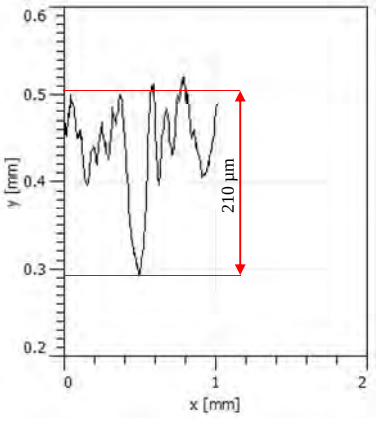

(c)

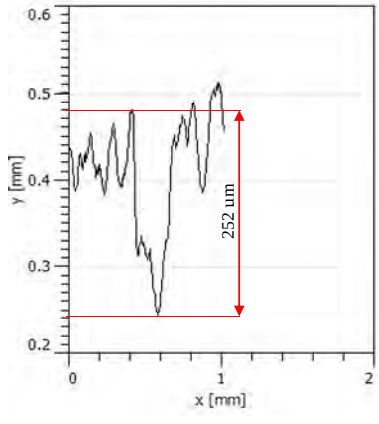

(d)

With a further augment in fluence from 2.29 to 2.54 J/cm^2, saturation in the hole depth is observed due to the formation of the plasma plume at a larger fluence of 2.54 J/cm^2 by ionising the material surface. As the hole depth gets deeper, a part of the plasma is entrapped inside the drilled hole. As a result, a fraction of the energy is absorbed by the trapped plasma plume inside the hole (Zhang et al., 2015). Due to this, saturation in depth is observed for nested concentric and Z-path. Also, the multiple reflections of the laser beam inside the hole lead to the absorption of laser energy by the hole wall surface, reducing the laser energy for further material removal (Zhang et al., 2015). The topography of the hole formed at 2.54 J/cm^2, 50 kHz for nested concentric and Z-path mode is illustrated in Figure 5, which shows that, the Z-path achieves a hole depth of 20% higher than that of the nested concentric. The relationship of laser fluence with hole

depth illustrated in Figure 4 is in line with the previously reported results of the micro-machining of TBC (Marimuthu et al., 2020).

Figure 4 elucidates that the SCD increases with an increase in laser fluence. At 1.78 J/cm^2, the SCD of 0.0034 and 0.0059 µm/µm^2 are obtained for nested concentric and Z-path. Because the thermal gradient developed during material processing at low laser fluence is minimum, resulting in minimal SCD. An increase in fluence to 2.54 J/cm^2, a SCD of 0.0079 and 0.0119 µm/µm^2 are noticed for nested concentric and Z-path, respectively. The material surface absorbs more laser energy, which causes a large temperature gradient on the TBC, leading to increased SCD (Parthiban et al., 2018). The Z-path has a higher SCD than the nested concentric path because more laser energy is imparted onto the material surface due to the Z-type motion of the laser beam.

Figure 6 Hole morphology at various fluence for nested concentric and Z-path, (a) 1.78 J/cm^2, (b) 2.04 J/cm^2, (c) 2.29 J/cm^2, (d) 2.54 J/cm^2 (see online version for colours)

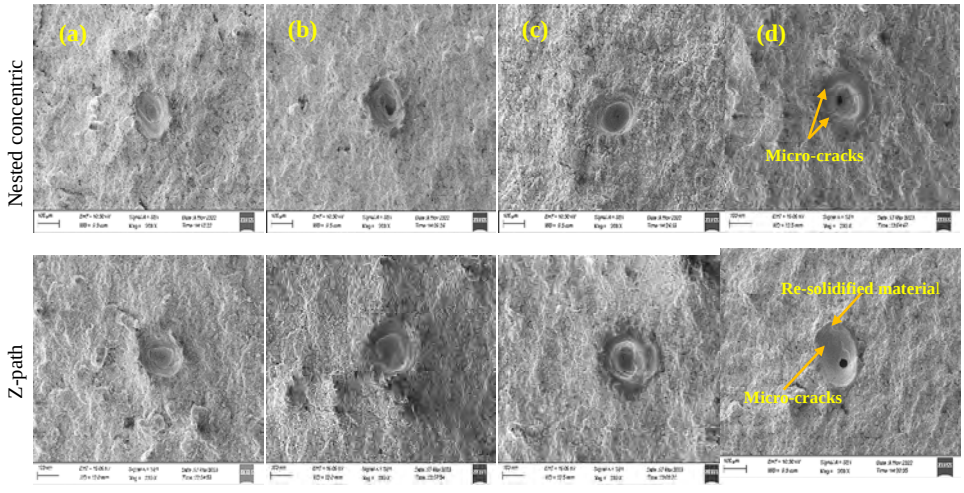

Figure 7 Hole diameter vs. repetition rate at various scanning paths, (a) nested concentric path, (b) Z-path (see online version for colours)

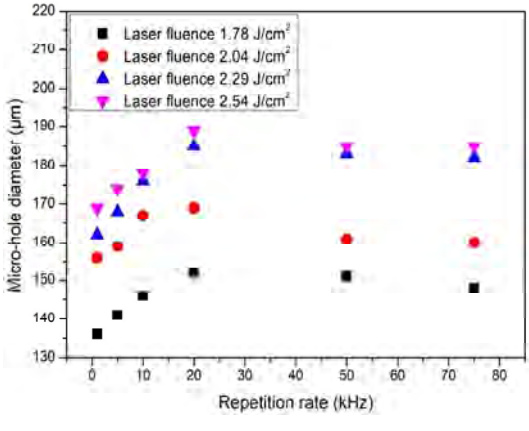

(a)

Figure 7 Hole diameter vs. repetition rate at various scanning paths, (a) nested concentric path, (b) Z-path (continued) (see online version for colours)

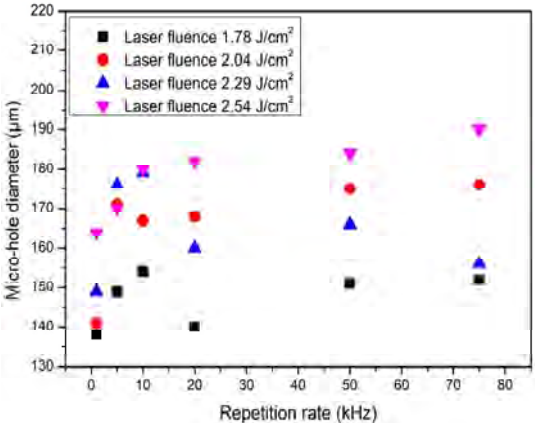

(b)

Figure 6 illustrates the hole morphology drilled at various laser fluence for Z-path and nested concentric paths. As demonstrated in Figures 6(a) and 6(b), from 1.78 J/cm^2 to 2.04 J/cm^2, micro-cracks, and re-solidified layers are not observed for nested concentric and Z-path scanning paths. An increased influence from 2.29 to 2.54 J/cm^2 resulted in a re-solidified molten layer and micro-cracks for both the scanning paths, as shown in Figure 6(d). This is due to the strong ablation that caused molten material ejection during the plasma expansion. This molten material cools down instantly and re-solidifies near the hole, forming defects such as recast layer and spatter deposition.

3.3 Effect of repetition rate on SCD, morphology, and hole dimension

To understand the effect of RR on micro hole dimensions (diameter and depth) and SCD, the RR is varied from 1 to 75 kHz, as given in Table 4. An increase in RR from 1 to 20 kHz for nested concentric and from 1 to 10 kHz for Z-path resulted in an increase in micro hole diameter irrespective of laser fluence, as shown in Figures 7(a) and 7(b), respectively. This is because as RR increases, the time for cooling the molten material is very short, which leads to an increase in temperature, thereby increasing the ablation rate, resulting in a larger hole diameter. At CRR of 20 kHz, the highest hole diameters of 152, 169, 189, and 192 µm are obtained for 1.78, 2.04, 2.29, and 2.54 J/cm^2, respectively, and saturation in the ablation is noticed at a repetition rate for nested concentric path (Zhao et al., 2020). On the contrary, for Z-path scanning mode, the highest hole diameters of 154, 167, 179 µm, and 180 µm are obtained for 1.78, 2.04, 2.29, and 2.54 J/cm^2, respectively, at CRR of 10 kHz. Subsequently, a decrease in hole diameter is observed for various fluence due to ablation threshold saturation. In addition, as the RR increases from 20 to 75 kHz, the separation gap between the laser pulse is significantly less for the complete ejection of the ablated material from the hole. This melted material re-solidifies around the hole periphery, thereby reducing the diameter. A similar phenomenon is noticed while drilling a micro hole using an ultra-short laser on TBC-coated nickel alloy (Liu et al., 2020).

Table 4 Variation of microhole dimensions and SCD with different repetition rate

S. no.	RR (kHz)	Scanning path	At 1.78 J/cm^2			At 2.04 J/cm^2			At 2.29 J/cm^2			At 2.54 J/cm^2		
			Hole diameter (μm)	Hole depth (μm)	SCD (μm/μm^2)	Hole diameter (μm)	Hole depth (μm)	SCD (μm/μm^2)	Hole diameter (μm)	Hole depth (μm)	SCD (μm/μm^2)	Hole diameter (μm)	Hole depth (μm)	SCD (μm/μm^2)
1	1	Nested concentric	136	204	0.0015	156	220	0.0022	162	234	0.055	169	240	0.0059
		Z-path	138	220	0.0082	141	235	0.0087	149	238	0.0099	164	240	0.0101
2	5	Nested concentric	141	206	0.0018	159	229	0.0033	168	241	0.006	174	257	0.0073
		Z-path	149	238	0.0086	171	243	0.0088	176	246	0.0107	170	241	0.011
3	10	Nested concentric	146	212	0.0027	167	234	0.0038	176	245	0.0063	178	258	0.0075
		Z-path	154	246	0.0089	167	249	0.0099	179	257	0.0117	180	258	0.0119
4	20	Nested concentric	152	221	0.0034	169	239	0.0042	185	247	0.0065	189	257	0.0079
		Z-path	140	235	0.0087	168	238	0.0088	160	243	0.0094	182	248	0.0109
5	50	Nested concentric	151	237	0.0048	161	244	0.0050	183	246	0.0076	185	252	0.0084
		Z-path	151	234	0.0091	175	236	0.0093	166	190	0.0103	184	249	0.0105
6	75	Nested concentric	148	242	0.0045	160	245	0.0051	182	246	0.0074	185	255	0.0081
		Z-path	152	239	0.0097	176	249	0.0099	156	198	0.0113	190	253	0.0116

Figure 8 Hole depth vs. repetition rate at various scanning paths, (a) nested concentric path, (b) Z-path (see online version for colours)

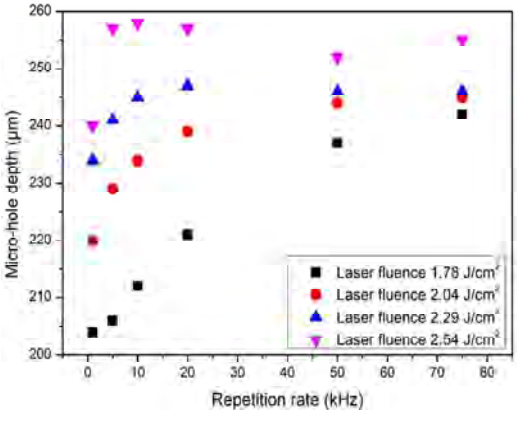

(a)

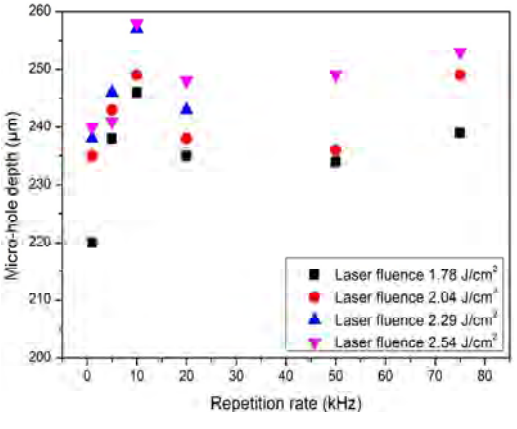

(b)

From Figures 8(a) and 8(b), it is observed that an increase in RR resulted in increased hole depth up to a critical RR of 20 kHz for nested concentric and 10 kHz for Z-path at various fluence. At an RR of 1 kHz, the minimum hole depth of 204, 220, 234, and 240 µm is observed for the nested concentric scanning path at 1.78, 2.04, 2.29, and 2.54 J/cm^2, respectively. For Z-path movement, the minimum hole depth of 220, 235, 238, and 240 µm is observed for 1.78, 2.04, 2.29, and 2.54 J/cm^2, respectively. Because the pulse-off time between the subsequent laser pulses is too long at a lower repetition rate, resulting in low material removal from the workpiece to form a shallow hole. As the RR increases, more energy is available to ablate the material to form a deeper hole. Compared to the nested concentric path, the Z-path generates a hole with a depth of 15 µm more than the nested concentric path due to infusion of more laser energy. After the critical RR of 20 kHz and 10 kHz for nested concentric and Z-path, saturation in the hole depth is observed till 75 kHz for all laser fluence. This is because, as the RR increases, ejection time between the pulses reduces, which accumulates more debris inside the hole wall (Yang et al., 2020). This resolidified material absorbs a part of

upcoming laser energy, thus inhibiting further penetration of the hole depth. Moreover, the energy reaching the bottom of the hole decreases at higher laser pulses due to the accumulation of more laser energy on the hole wall surface (Zhang et al., 2024). This result is in line with micro-hole drilling of titanium carbide using a femtosecond laser (Zhang et al., 2015).

Figure 9 SCD vs. repetition rate at various scanning paths, (a) nested concentric path, (b) Z-path (see online version for colours)

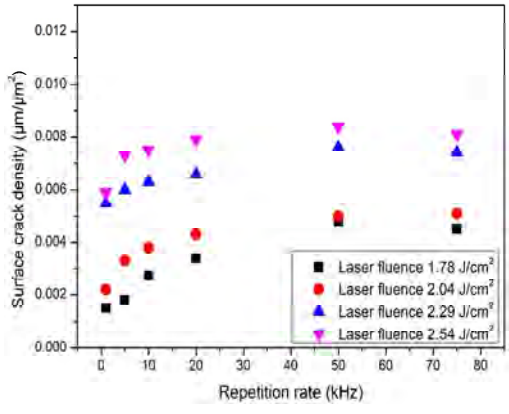

(a)

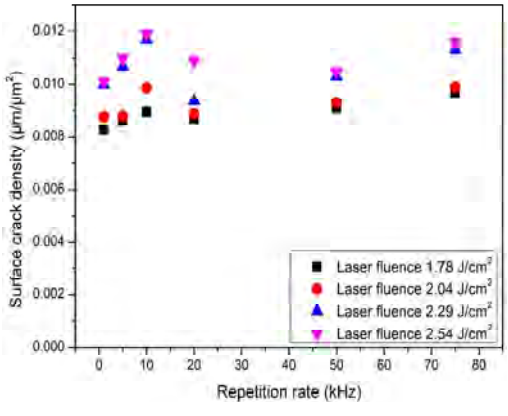

(b)

Figure 9 demonstrates the effect of RR on SCD at various laser fluence for nested concentric and Z-path. As the RR increases from 1 to 20 kHz, SCD increases from all the laser fluence, as shown in Figure 9. At a lower RR of 1 kHz, the temporal separation gap among the pulses is large enough so that the temperature gradient near the hole entrance is significantly less; as a result, the surface crack is limited. Further increase of RR to a CRR, (i.e., 20 kHz and 10 kHz) for nested concentric and Z-path resulted in increased SCD for various laser fluence due to the rapid heating and cooling effect. This leads to a significant temperature gradient on the hole surface, resulting in higher SCD (Morar et al., 2018). A decrease in SCD is observed after a critical RR of 20 and 10 kHz for nested concentric and Z-path due to the saturation in the ablation threshold.

Table 5 Variation of microhole dimensions and SCD with different pulse overlap

S. no.	*PO (%)*	*Scanning path*	*At 1.78 J/cm²*			*At 2.04 J/cm²*			*At 2.29 J/cm²*			*At 2.54 J/cm²*		
			Hole diameter (μm)	*Hole depth (μm)*	*SCD (μm/μm²)*	*Hole diameter (μm)*	*Hole depth (μm)*	*SCD (μm/μm²)*	*Hole diameter (μm)*	*Hole depth (μm)*	*SCD (μm/μm²)*	*Hole diameter (μm)*	*Hole depth (μm)*	*SCD (μm/μm²)*
1	75	Nested concentric	207	212	0.0091	227	235	0.0105	230	240	0.0111	235	250	0.0115
		Z-path	215	217	0.0077	245	247	0.0122	258	248	0.0149	263	234	0.0162
2	50	Nested concentric	197	210	0.006	211	223	0.0088	207	230	0.0093	208	243	0.0098
		Z-path	202	212	0.0071	234	238	0.0099	249	241	0.0114	259	215	0.0112
3	25	Nested concentric	193	190	0.004	208	214	0.0074	198	224	0.0078	198	226	0.008
		Z-path	192	219	0.005	221	219	0.0067	227	231	0.0097	228	204	0.01
4	0	Nested concentric	195	168	0.002	210	188	0.004	193	192	0.0073	195	203	0.008
		Z-path	158	176	0.003	176	176	0.0067	196	191	0.0077	205	197	0.0083

Figure 10 shows the hole morphology at various RR and laser fluence for nested concentric and Z-path scanning. No significant change in hole morphology is noticed with an increased RR at a fluence of 1.78 J/cm^2 for nested concentric and Z-path scanning. Spatter is observed at 1.78 J/cm^2 with a high RR of 50 kHz for both the scanning paths, as depicted in Figure 10. At 2.54 J/cm^2, spatter and micro-cracks are visible near the hole at 50 kHz for nested concentric and Z-path.

Figure 10 Hole morphology at various RR for nested concentric and Z-path (see online version for colours)

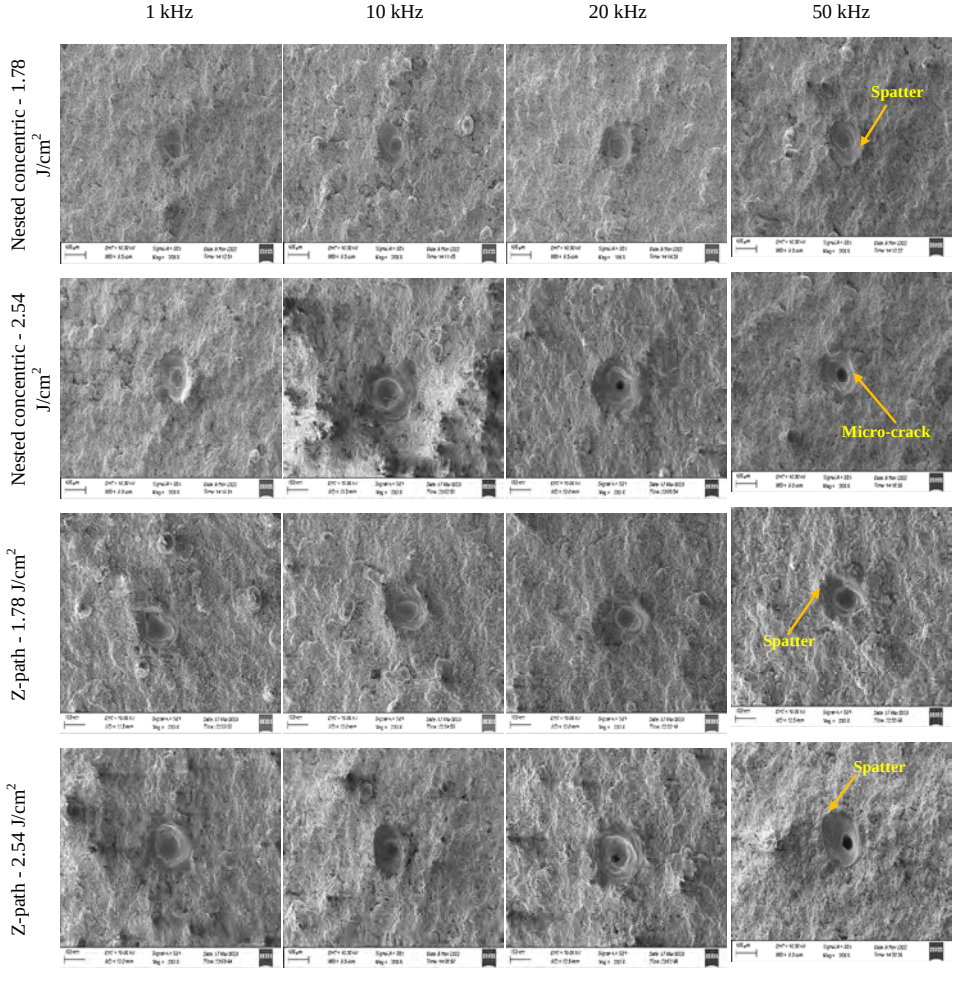

Figure 11 Hole diameter vs. pulse overlap at various scanning paths, (a) nested concentric path, (b) Z-path (see online version for colours)

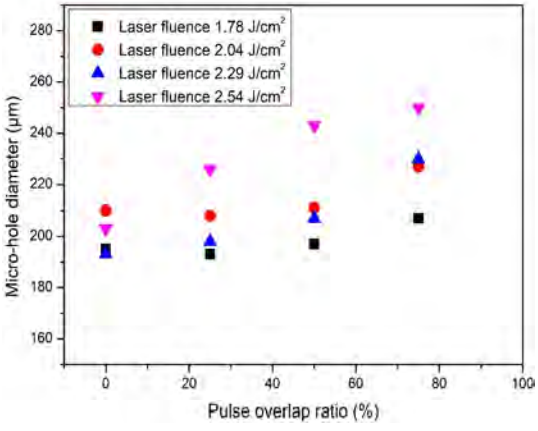

(a)

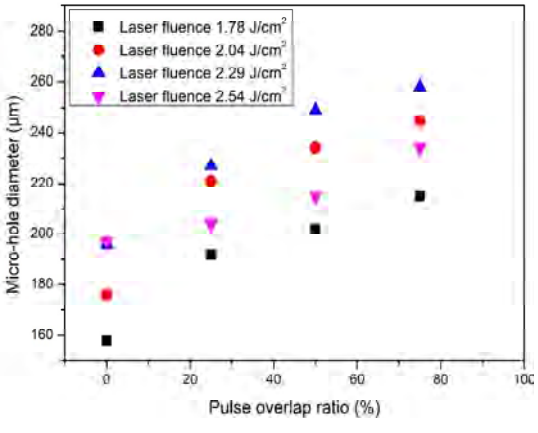

(b)

3.4 Effect of pulse overlap on SCD, morphology, and hole dimension

It is evident from the graph that, with an increase in pulse overlap (PO) from 0% to 75%, the hole diameter, depth, and SCD increased with different laser fluence for nested concentric and Z-path, as illustrated in Figures 11, 12 and 13, respectively. Due to the absence of overlap at SS of 400 mm/s, the interaction time on the hole decreases correspondingly, reducing the laser energy input, which leads to the formation of a shallow hole with a smaller hole diameter and the minimum amount of SCD due to less temperature gradient. A similar trend is observed for Z-path and nested concentric paths, irrespective of laser fluence. In addition, the material ablation gets weakened, leading to slower material evaporation and reduced ablation of atoms within the time period, leading to the shrinkage in the dimensions of the micro holes (Dong et al., 2024). As the pulse overlap increases from 25% to 75%, a significant increase in the hole diameter, depth, and SCD is noticed for nested concentric and Z-path, as demonstrated in

Figures 11, 12, and 13, respectively. As PO increases, the interaction time between the pulses on the material surface increases, thereby increasing the machining time, which leads to the ablating of more material from the desired spot (Sun et al., 2019). Hence, the hole diameter and depth for both the scanning paths increased. A similar result for micro hole dimension is witnessed during laser micro-drilling of aluminium alloy coated with titanium diboride/zirconium diboride (Mahamani et al., 2017). The variation of micro hole diameter, depth and SCD with different pulse overlap ratio is given in Table 5.

Figure 12 Hole depth vs. pulse overlap at various scanning paths, (a) nested concentric path, (b) Z-path (see online version for colours)

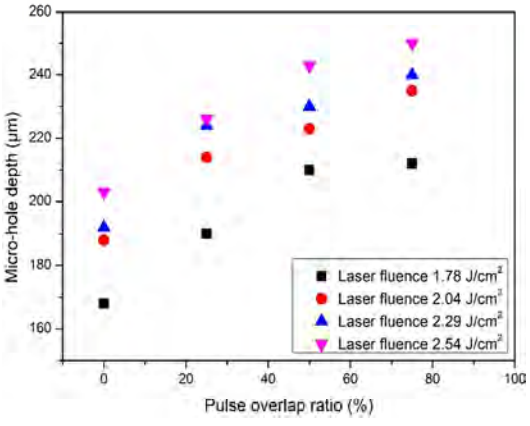

(a)

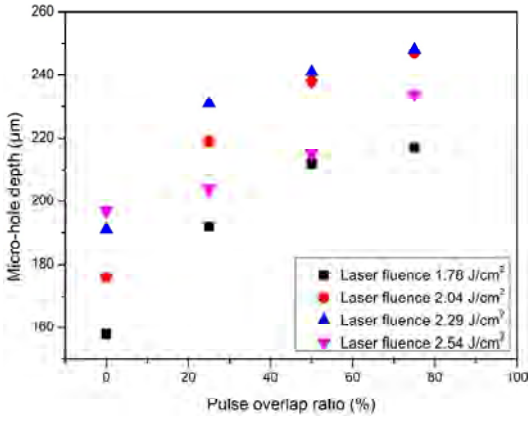

(b)

The hole morphology at various PO for nested concentric and Z-path is demonstrated in Figure 14. The SEM image of the microhole at 1.78 J/cm^2 for 0% pulse overlap resulted in the formation of a shallow hole for nested concentric and Z-path because of less laser energy available to ablate the TBC. At 1.78 and 2.54 J/cm^2 with 75% overlap, spatter and micro-cracks are noticed for both paths at the hole edge due to immense heat accumulation on the work material surface. Moreover, spatter and micro-crack are noticed for the Z-path for 25 and 50% PO at 2.54 J/cm^2, respectively.

Table 6 Variation of microhole dimensions and SCD with repeated laser scans

S. no.	*No. of laser scans*	*Scanning path*	*At 1.78 J/cm²*			*At 2.04 J/cm²*			*At 2.29 J/cm²*			*At 2.54 J/cm²*		
			Hole diameter (μm)	*Hole depth (μm)*	*SCD (μm/μm²)*	*Hole diameter (μm)*	*Hole depth (μm)*	*SCD (μm/μm²)*	*Hole diameter (μm)*	*Hole depth (μm)*	*SCD (μm/μm²)*	*Hole diameter (μm)*	*Hole depth (μm)*	*SCD (μm/μm²)*
1	1	Nested concentric	145	190	0.0044	164	193	0.0059	170	211	0.0071	178	222	0.0079
		Z-path	162	193	0.0013	170	196	0.0049	175	227	0.0109	182	235	0.0087
2	50	Nested concentric	162	198	0.0058	168	211	0.0062	172	223	0.0073	183	237	0.0084
		Z-path	185	210	0.0042	189	232	0.0053	219	241	0.0111	240	269	0.0141
3	100	Nested concentric	173	210	0.0063	187	232	0.0075	192	240	0.0089	202	243	0.0091
		Z-path	187	229	0.0075	193	239	0.0065	234	246	0.0195	287	275	0.0162
4	150	Nested concentric	185	234	0.0079	208	238	0.0082	212	251	0.0092	208	256	0.0094
		Z-path	207	240	0.0097	212	247	0.0082	290	255	0.0153	313	278	0.0172
5	200	Nested concentric	190	248	0.0085	214	254	0.0087	210	259	0.0095	229	263	0.0097
		Z-path	208	251	0.011	213	249	0.0108	290	269	0.0132	330	280	0.0178

Figure 13 SCD vs. pulse overlap at various scanning paths, (a) nested concentric path, (b) Z-path (see online version for colours)

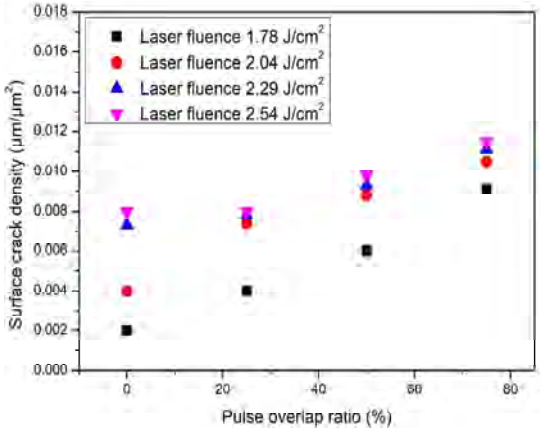

(a)

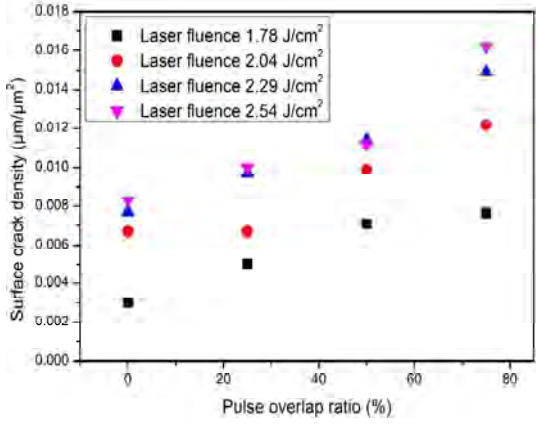

(b)

3.5 Effect of number of repeated laser scans on SCD, morphology, and hole dimension

The influence of number of repeated scans on hole diameter, depth, and SCD for nested concentric and Z-path at various laser fluence are shown in Table 6. It indicates that as the laser scan increases, the diameter, depth, and SCD increase, irrespective of laser fluence due to heat accumulation. During single-time laser scanning, the heat generated on the surface of the TBC has sufficient time for cooling after the ablation process. Moreover, heat generated on the material surface is less than enough to ablate the material. This results in forming a shallow hole with a smaller diameter hole with the lowest SCD for all the laser fluence for both the scanning paths, as illustrated in Figures 15, 16, and 17.

Figure 14 Hole morphology at various pulse overlap for nested concentric and Z-path (see online version for colours)

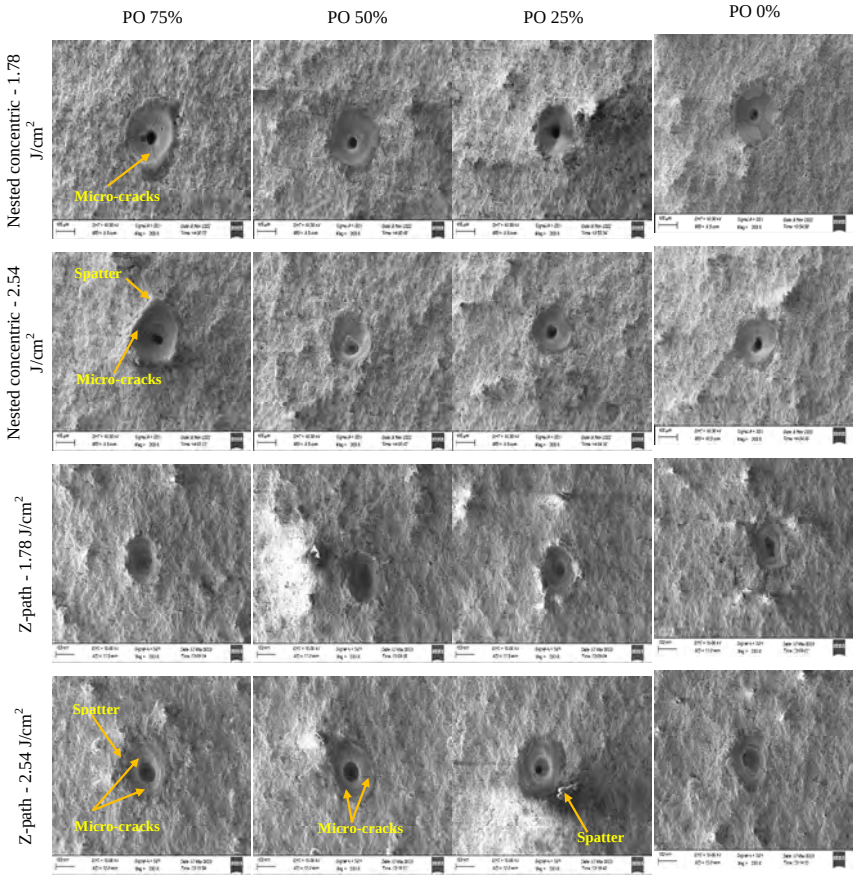

Figure 15 Hole diameter vs. no. of laser scans at various scanning paths, (a) nested concentric path, (b) Z-path (see online version for colours)

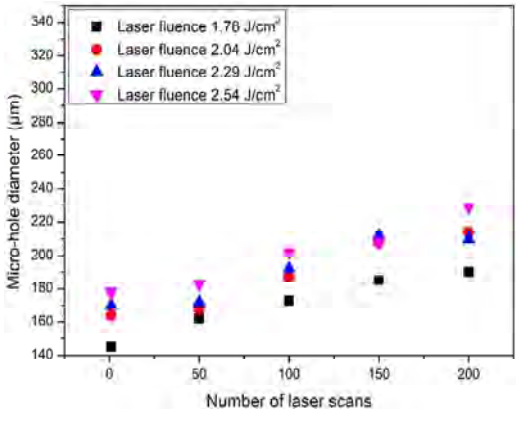

(a)

Figure 15 Hole diameter vs. no. of laser scans at various scanning paths, (a) nested concentric path, (b) Z-path (continued) (see online version for colours)

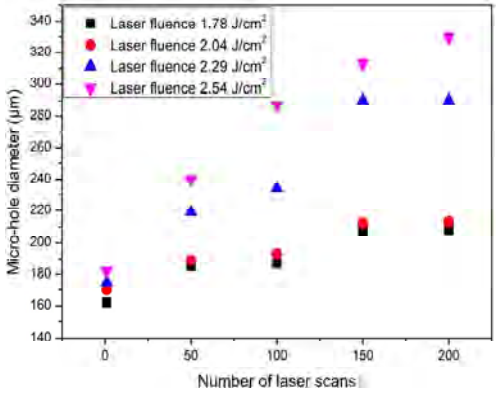

(b)

Figure 16 Hole depth vs. no. of laser scans at various scanning paths, (a) nested concentric path, (b) Z-path (see online version for colours)

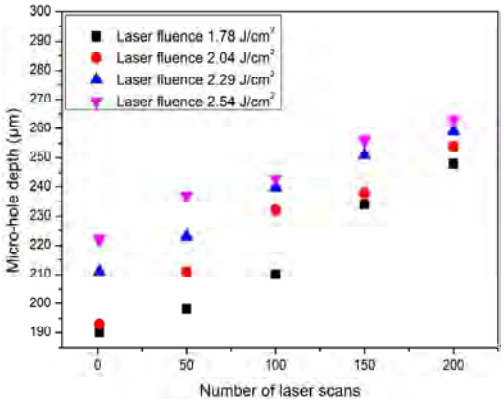

(a)

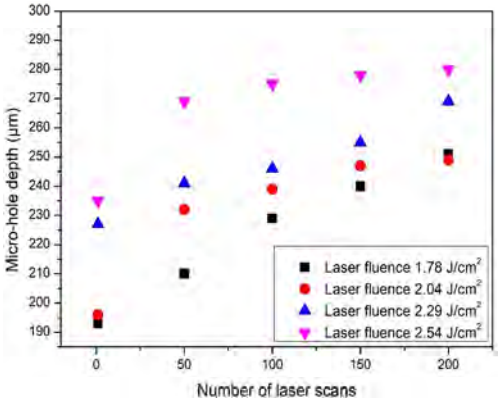

(b)

Figure 17 SCD vs. no. of laser scans at various scanning paths, (a) nested concentric path, (b) Z-path (see online version for colours)

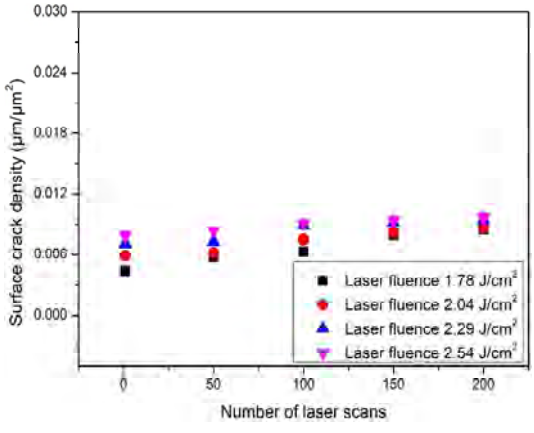

(a)

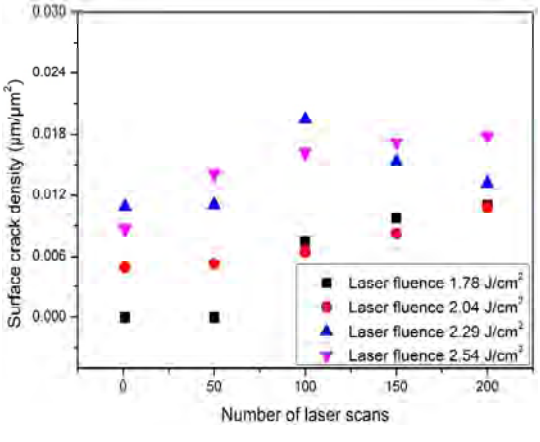

(b)

As the number of laser scans increases from 50 to 200, an increase in hole diameter, depth, and SCD is noticed. Because the heat generated during the process increases with increased laser scans. In addition, as the laser scan increases, accumulated laser-induced thermal stresses lead to material cracking due to a high thermal gradient and insufficient cooling time after each laser scan (Parthiban et al., 2018). A similar result was obtained by laser micro-machining of thermal barrier coated nickel alloy (Marimuthu et al., 2020). Moreover, the Z-path induces more surface cracks than the nested concentric path.

The SEM image in Figure 18 demonstrates the hole morphology for nested concentric and Z-path at various fluence and number of laser scans. For a single scan, the hole morphology is free from micro-cracks and spatter for various laser fluence. Spatter is noticed near the hole entrance at 1.78 J/cm^2 with 200 laser scans for nested concentric and Z-path. At 2.54 J/cm^2, spatter and micro-cracks are observed for 100 and 200 laser scans, irrespective of the scanning path.

Figure 18 Hole morphology at various laser fluence and number of laser scan (see online version for colours)

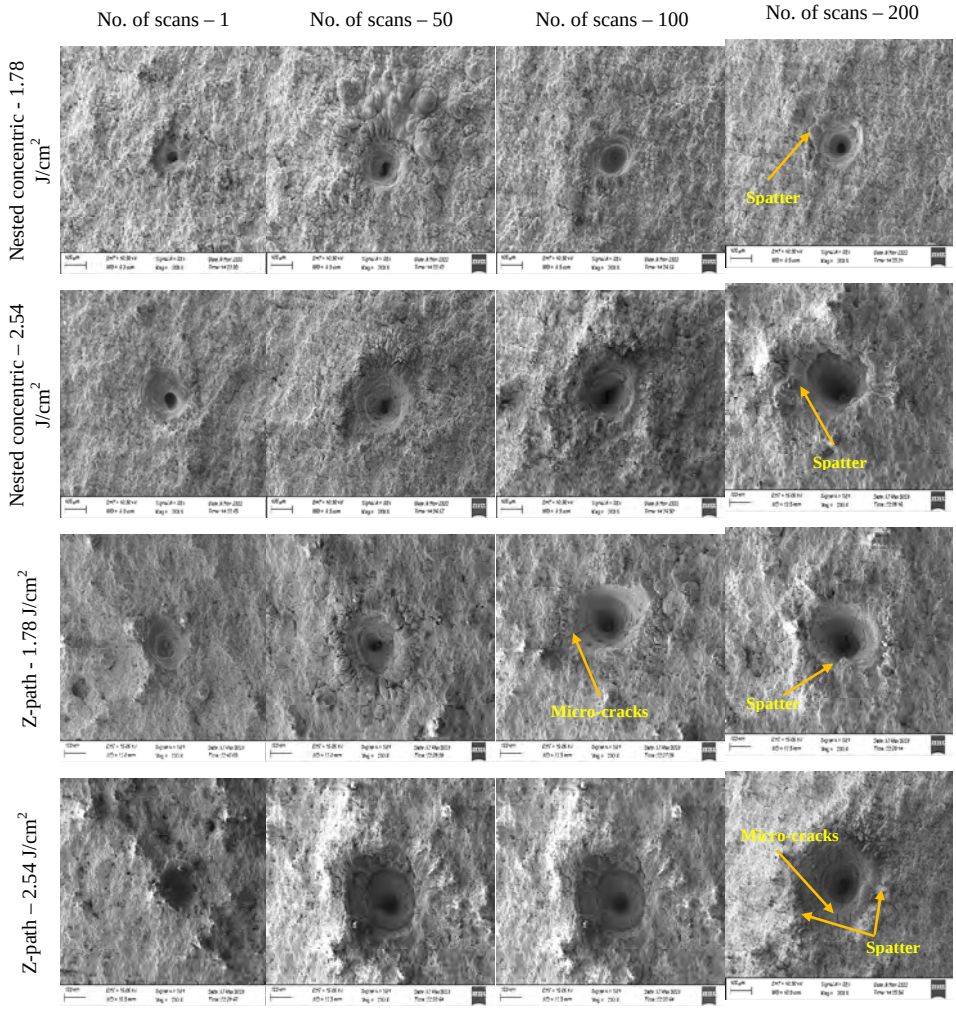

4 Conclusions

An in-depth experimental investigation has been performed to ablate micro holes on TBC titanium alloy using ultrashort pulse laser operating in femtosecond regime. By examining the variations in micro hole dimensions, hole morphology and SCD with respect to laser process parameters such as PO, RR, laser fluence and number of laser scans, the following conclusions were drawn:

- Regardless of changes in laser fluence, a declining trend in threshold fluence is observed up to the critical RR of 20 kHz for nested concentric and 10 kHz for Z-scanning path. At critical RR, improved hole morphology is observed with less microcracks and spatter.

- While a Z-path can produce micro holes with 20% more depth than those produced by the nested concentric approach at a fluence of 2.54 J/cm^2, a nested concentric scanning path is the best approach for manufacturing precise micro holes.
- The largest hole dimension and surface fracture density are found at higher laser fluence of 2.29 J/cm^2 because of strong ablation mechanism regardless of scanning path. Beyond this point, the growth rate declines due to the plasma shielding effect.
- The micro hole dimensions and SCD escalates as PO and the number of laser scans increases, regardless of variation in fluence and scanning techniques, due to inadequate heat dissipation by the TBC. An optimal hole morphology is achieved with a PO of 25% and of 100 laser scans.

4.1 Limitation of the present work

- Presently available femtosecond laser micromachining centre cannot produce micro holes in materials with higher thicknesses.
- The existing Galvano scanner system does not support double rotation and interlaced scanning methods.
- With the present femtosecond laser micromachining centre, investigations into the effect of varying pulse duration on micro hole sizes and hole shape are not feasible due to the fixed pulse width of 350 fs.

References

Bandyopadhyay, S., Sarin Sundar, J.K., Sundararajan, G. and Joshi, S.V. (2002) 'Geometrical features and metallurgical characteristics of Nd:YAG laser drilled holes in thick IN718 and Ti-6Al-4V sheets', *Journal of Materials Processing Technology*, Vol. 127, pp.83–95, https://doi.org/10.1016/S0924-0136(02)00270-4.

Bathe, R. and Padmanabham, G. (2014) 'Evaluation of laser drilling of holes in thermal barrier coated superalloys', *Materials Science and Technology (United Kingdom)*, Vol. 30, pp.1778–1782, https://doi.org/10.1179/1743284713Y.0000000477.

Bhattacharyya, B., Gangopadhyay, S. and Sarkar, B.R. (2007) 'Modelling and analysis of EDMED job surface integrity', *Journal of Materials Processing Technology*, Vol. 189, pp.169–177, https://doi.org/10.1016/j.jmatprotec.2007.01.018.

Biffi, C.A. and Previtali, B. (2013) 'Spatter reduction in nanosecond fibre laser drilling using an innovative nozzle', *International Journal of Advanced Manufacturing Technology*, Vol. 66, pp.1231–1245, https://doi.org/10.1007/s00170-012-4402-y.

Clarke, D.R. and Phillpot, S.R. (2005) 'Thermal barrier coating materials', *Materials Today*, Vol. 8, pp.22–29, https://doi.org/10.1016/S1369-7021(05)70934-2.

Das, D.K. and Pollock, T.M. (2009) 'Femtosecond laser machining of cooling holes in thermal barrier coated CMSX4 superalloy', *Journal of Materials Processing Technology*, Vol. 209, pp.5661–5668, https://doi.org/10.1016/j.jmatprotec.2009.05.031.

Das, D.K., McDonald, J.P., Yalisove, S.M. and Pollock, T.M. (2008) 'Femtosecond pulsed laser damage characteristics of 7% Y2O 3-ZrO2 thermal barrier coating', *Applied Physics A: Materials Science and Processing*, Vol. 91, pp.421–428, https://doi.org/10.1007/s00339-008-4417-2.

DeMasi-Marcin, J.T. and Gupta, D.K. (1994) 'Protective coatings in the gas turbine engine', *Surface and Coatings Technology*, Vols. 68–69, pp.1–9, https://doi.org/10.1016/0257-8972(94)90129-5.

Di Niso, F., Gaudiuso, C., Sibillano, T. et al. (2014) 'Role of heat accumulation on the incubation effect in multi-shot laser ablation of stainless steel at high repetition rates', *Optics Express*, Vol. 22, p.12200, https://doi.org/10.1364/oe.22.012200.

Dong, Y., Shao, P., Guo, X. et al. (2024) 'Experimental study on the effect of laser overlap rate on the quality of femtosecond laser machining of micro-holes', *Optics and Laser Technology*, Vol. 177, https://doi.org/10.1016/j.optlastec.2024.111205.

Feng, Q., Picard, Y.N., McDonald, J.P. et al. (2006) 'Femtosecond laser machining of single-crystal superalloys through thermal barrier coatings', *Materials Science and Engineering A*, Vol. 430, pp.203–207, https://doi.org/10.1016/j.msea.2006.05.104.

Kelly, R. and Miotello, A. (1996) 'Comments on explosive mechanisms of laser sputtering', *Applied Surface Science*, Vols. 96–98, pp.205–215, https://doi.org/10.1016/0169-4332(95)00481-5.

Khadtare, A., Pawade, R., Varghese, A. and Joshi, S. (2020) 'Micro-drilling of straight and inclined holes on thermal barrier coated Inconel 718 for turbine blade cooling', *Materials and Manufacturing Processes*, Vol. 35, pp.783–796, https://doi.org/10.1080/10426914.2020.1740253.

Li, R., Zhou, W., Zhou, C. et al. (2022) 'Laser damage threshold of Ge8As23S69 films irradiated under single-and multiple-pulse femtosecond laser', *Ceramics International*, Vol. 48, pp.8341–8348, https://doi.org/10.1016/j.ceramint.2021.12.040.

Li, Z.Y., Wei, X.T., Guo, Y.B. and Sealy, M.P. (2015) 'State-of-art, challenges, and outlook on manufacturing of cooling holes for turbine blades', *Machining Science and Technology*, Vol. 19, pp.361–399, https://doi.org/10.1080/10910344.2015.1051543.

Liu, H., Zhao, W., Wang, L. et al. (2020) 'Percussion drilling of deep holes using picosecond ultrashort pulse laser in Ni-based superalloy coated with ceramic thermal barrier coatings', *Materials*, Vol. 13, https://doi.org/10.3390/MA13163570.

Liu, J.M. (1982) 'Simple technique for measurements of pulsed Gaussian-beam spot sizes', *Optics Letters*, Vol. 7, p.196, https://doi.org/10.1364/ol.7.000196.

Liu, Y., Zhang, R., Li, W. et al. (2018) 'Effect of machining parameter on femtosecond laser drilling processing on SiC/SiC composites', *The International Journal of Advanced Manufacturing Technology*, pp.1795–1811, https://doi.org/10.1007/s00170-017-1163-7.

Lu, C., Duan, W., Wang, K. et al. (2020) 'Experiments of drilling micro-holes on superalloy with thermal barrier coatings by using femtosecond laser', *Ferroelectrics*, Vol. 564, pp.37–51, https://doi.org/10.1080/00150193.2020.1761700.

Mahamani, A. and Anantha Chakravarthy, V.V. (2017) 'Investigation on laser drilling of AA6061-TiB2/ZrB2 in situ composites', *Materials and Manufacturing Processes*, Vol. 32, pp.1700–1706, https://doi.org/10.1080/10426914.2016.1244836.

Marimuthu, S., Smith, B., Kiely, A. and Liu, Y. (2020) 'Millisecond pulse laser machining of thermal barrier coatings', *CIRP Journal of Manufacturing Science and Technology*, Vol. 28, pp.107–117, https://doi.org/10.1016/j.cirpj.2019.11.004.

McNally, C.A., Folkes, J. and Pashby, I.R. (2004) 'Laser drilling of cooling holes in aeroengines: state of the art and future challenges', *Materials Science and Technology*, Vol. 20, pp.805–813, https://doi.org/10.1179/026708304225017391.

Meier, S.M. and Gupta, D.K. (1992) 'The evolution of thermal barrier coatings in gas turbine engine applications', *ASME 1992 International Gas Turbine and Aeroengine Congress and Exposition, GT 1992*, p.5, https://doi.org/10.1115/92GT203.

Morar, N.I., Roy, R., Mehnen, J. et al. (2018) 'Investigation of recast and crack formation in laser trepanning drilling of CMSX-4 angled holes', *International Journal of Advanced Manufacturing Technology*, Vol. 95, pp.4059–4070, https://doi.org/10.1007/s00170-017-1481-9.

Niu, J., Yang, J., Tan, J. et al. (2024) 'Study of the TBC delamination in nanosecond laser percussion drilling of inclined film cooling holes', *Optics and Laser Technology*, Vol. 169, https://doi.org/10.1016/j.optlastec.2023.110077.

Parthiban, K., Duraiselvam, M. and Manivannan, R. (2018) 'TOPSIS based parametric optimization of laser micro-drilling of TBC coated nickel based superalloy', *Optics and Laser Technology*, Vol. 102, pp.32–39, https://doi.org/10.1016/j.optlastec.2017.12.012.

Pawar, A., Kamble, D. and Jadhav, D.B. (2024) 'Experimental investigation on titanium alloys for machining of stepped circular holes using ultrasonic-assisted hybrid ECM', *Journal of Engineering and Applied Science*, Vol. 71, No. 58, pp.1–19.

Perveen, A., Lutey, A.H.A., Romoli, L., Cucinotta, A. and Selleri, S. (2020) 'Pulsed machining of high-performance engineering and biomedical alloys', *Machining J.*, Vol. 22, No. 2, pp.137–152.

Sun, X., Dong, X., Wang, K. et al. (2019) 'Experimental investigation on thermal effects in picosecond laser drilling of thermal barrier coated In718', *Optics and Laser Technology*, Vol. 113, pp.150–158, https://doi.org/10.1016/j.optlastec.2018.12.020.

Voisey, K.T. and Clyne, T.W. (2004) 'Laser drilling of cooling holes through plasma sprayed thermal barrier coatings', *Surface and Coatings Technology*, Vol. 176, pp.296–306, https://doi.org/10.1016/S0257-8972(03)00748-5.

Yang, Z., Ji, P., Zhang, Z. et al. (2020) 'Fundamental 3D simulation of the femtosecond laser ablation for cooling hole drilling on Ni and Fe based aero-engine components', *Optics Communications*, Vol. 475, https://doi.org/10.1016/j.optcom.2020.126237.

Yeo, C.Y., Tam, S.C., Jana, S. and Lau, M.W.S. (1994) 'A technical review of the laser drilling of aerospace materials', *Journal of Materials Processing Tech.*, Vol. 42, pp.15–49, https://doi.org/10.1016/0924-0136(94)90073-6.

Yu, Z., Hu, J. and Li, K. (2019) 'Investigating the multiple-pulse drilling on titanium alloy in picosecond laser', *Journal of Materials Processing Technology*, Vol. 268, pp.10–17, https://doi.org/10.1016/j.jmatprotec.2018.12.027.

Zhai, Z., Wang, W., Zhao, J. et al. (2017) 'Influence of surface morphology on processing of C/SiC composites via femtosecond laser', *Composites Part A: Applied Science and Manufacturing*, Vol. 102, pp.117–125, https://doi.org/10.1016/j.compositesa.2017.07.031.

Zhang, H.D., Yu, H., Ning, J. et al. (2024) 'Experimental research on micro-drilling of refractory material tungsten by multi-pulse femtosecond laser ablation', *Optics and Laser Technology*, Vol. 168, https://doi.org/10.1016/j.optlastec.2023.109962.

Zhang, Y., Wang, Y., Zhang, J. et al. (2015) 'Micromachining features of TiC ceramic by femtosecond pulsed laser', *Ceramics International*, Vol. 41, pp.6525–6533, https://doi.org/10.1016/j.ceramint.2015.01.095.

Zhang, Z., Wang, W., Jiang, R. et al. (2020) 'Investigation on geometric precision and surface quality of microholes machined by ultrafast laser', *Optics and Laser Technology*, Vol. 121, p.105834, https://doi.org/10.1016/j.optlastec.2019.105834.

Zhao, W., Shen, X., Liu, H., Wang, L. and Jiang, H. (2020) 'Effect of high repetition rate on dimension and morphology of micro-hole drilled in metals by picosecond ultra-short pulse laser', *Optics and Lasers in Engineering*, Vol. 124, pp.1–8, https://doi.org/10.1016/j.optlaseng.2019.105811.

Zhao, W., Wang, W., Jiang, G. et al. (2015) 'Ablation and morphological evolution of micro-holes in stainless steel with picosecond laser pulses', *International Journal of Advanced Manufacturing Technology*, Vol. 80, pp.1713–1720, https://doi.org/10.1007/s00170-015-7145-8.